International Astronomical Union, Tucson, Ariz., March 8–10, 1971; also, *Physical Studies of Minor Planets*, edited by T. Gehrels, NASA SP-267, 1971.

[15] Forward, R. L., "Asteroid Mass Distribution Measurement With Gravity Gradiometers," *12th Colloquium of the International Astronomical Union*, Tucson, Ariz., March 8–10, 1971; also, *Physical Studies of Minor Planets*, edited by T. Gehrels, NASA SP-267, 1971.

[16] Forward, R. L., "Gravitational Field Measurements of Planetary Bodies with Gravity Gradient Instrumentation," Rept. 448, Aug. 1971, Hughes Research Lab., Malibu, Calif.

[17] Marsden, B. G., "Precision of Ephemerides for Space Missions," *12th Colloquium of the International Astronomical Union*, Tucson, Ariz., March 8–10, 1971; also, *Physical Studies of Minor Planets*, edited by T. Gehrels, NASA SP-267, 1971.

SEPTEMBER 1973 J. SPACECRAFT VOL. 10, NO. 9

Design of Graphite Nosetips for Ballistic Re-Entry

P. J. SCHNEIDER,* R. D. TETER,† W. D. COLEMAN,‡ AND R. M. HEATH§
Lockheed Missiles & Space Company Inc., Sunnyvale, Calif.

Analyses are given for re-entry shape change and indepth thermal/structural response of contemporary low-recession graphite nosetips. Both blunt plug configurations and sharp and blunt shell designs are treated from the principal viewpoint of surviving thermally induced tensile strains. Parametric calculations demonstrate the magnitude and variation in these re-entry thermal strains and their sensitivity to initial re-entry conditions and to various thermal and mechanical modeling elements in the design analysis sequence. In addition to thermal strain, a number of other design problems peculiar to graphite nosetips are discussed in their relationship to over-all re-entry vehicle thermal/structural capability.

Nomenclature

B_w' = mass-transfer parameter
c = specific heat, Btu/lb-°F
d = nosetip overhang radius, ft
E = elastic modulus, lb/in^2.
g = acceleration of gravity, ft/sec^2
H = enthalpy, Btu/lb
h = heat-transfer coefficient, lb/sec-ft^2
k = thermal conductivity, Btu/sec-ft-°F
M = Mach number
m = mass, lb
p = pressure, atm
Q = total convective heat load, Btu/ft^2
q = instantaneous heat rate, Btu/sec-ft^2
$\bar{q}$ = dynamic pressure, atm
R = radius of curvature, ft
Re = Reynolds number
R_N = nosetip radius, ft
r = radial coordinate (from centerline)
$\dot{s}$ = surface recession rate, fps
s = total stagnation-point recession, ft
t = temperature, °F
V_E = re-entry velocity, fps
x = axial coordinate (from stagnation point)
y = normal distance from original heatshield surface, ft
z = altitude, ft
β = thermal-expansion coefficient, in/in.-°F
$\bar{\beta}$ = ballistic coefficient, lb/ft^2
Γ = permeability, ft^2
γ_E = re-entry angle, deg
δ = nosetip overhang length, ft; deflection, ft
ε = thermal strain, %
ζ = mechanical erosion amplification factor = $\dot{s}_{\text{total}}/\dot{s}_{\text{chem}}$
θ = time, sec
λ = re-entry parameter = $(V_E^2/g)(\bar{\beta}/\rho_0 R_N^3 \sin\gamma_E)^{1/2} x 10^{-10}$
ν = Poisson ratio
ρ = air density, lb/ft^3

Subscripts

c = cavity, critical (onset) value
chem = chemical
E = re-entry
e = boundary-layer edge value
hoop = hoop (circumferential) direction
N = nosetip
r = radial
$r-x$ = pitch plane
sp = stagnation point
t = tensile
x = axial
w = wall (surface or internal) value, wedge
0 = sea level
θ = momentum thickness

Presented as Paper 72-705 at the AIAA 5th Fluid and Plasma Dynamics Conference, Boston, Mass., June 26–28, 1972; submitted July 7, 1972; revision received May 7, 1973. The analyses reported here were supported under Air Force ABRES contracts, Space and Missile Systems Organization, Norton AFB, Calif.: RVTO-2B, F04701-68-C-0157 (1968–1971); NDAT, F04701-69-C-0237 (1969–1971); and BPD, F04701-71-C-0011 (1970–1972). The authors are pleased to credit L. Brick and R. E. Wilson as LMSC managers of the supporting contracts, and L. W. Gallagher, Y. J. Kaku, L. R. Reneau, and W. K. Skeehan as contributors to the design work described here.

Index categories: Thermal Modeling and Experimental Thermal Simulation; Optimal Structural Design.

* Staff Engineer, Engineering Technology.
† Group Engineer, Loads/Structures & Dynamics.
‡ Research Specialist, Aero-Thermodynamics.
§ Research Specialist, Loads/Structures & Dynamics.

Introduction

AN increasing number of unclassified technology papers have appeared in recent years on the subject of ballistic-re-entry nosetips. Some have considered reinforced plastics[1] and others reinforced carbon nosetip materials.[2,3] Papers dealing with graphite nosetips have concentrated primarily on shape change and thermal response[4–6] and with ground testing of materials and subscale nosetip configurations.[7–9]

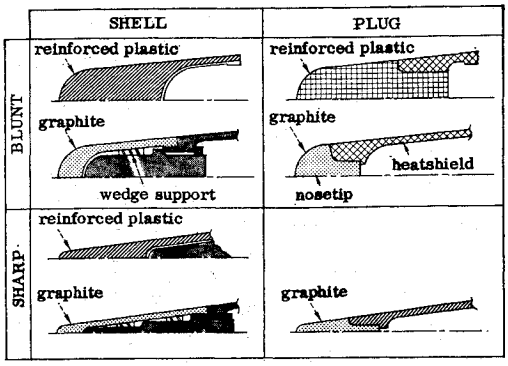

Fig. 1 Typical ballistic re-entry nosetips.

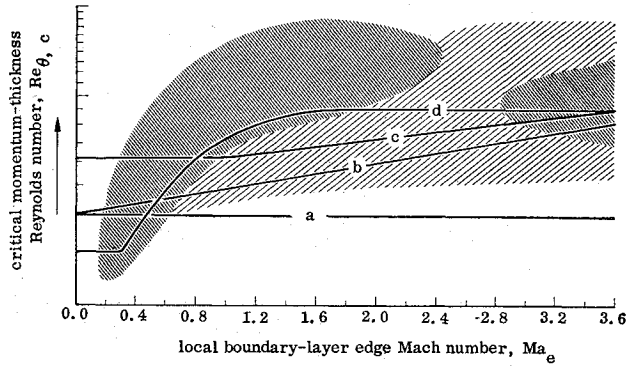

Fig. 2 Boundary-layer transition-onset models.

No complete work appears to treat the combined thermal/structural design problems of contemporary graphite nosetips.

The present paper analyzes axisymmetric graphite nosetips at zero angle of attack, using an established technology base and thermal/structural design methodology.[6,10] Typical response and sensitivity results are given for two specific classes of graphite nosetips, namely blunt plug designs and sharp and blunt shell configurations.

Figure 1 illustrates some general configurational features of reinforced-plastic and graphite nosetips for ballistic re-entry vehicles. In-flight structural failures of graphite nosetips can result from adverse shape-change effects (nosetip and heatshield), thermal-expansion mismatches, and fracture of the brittle graphite caused by excessive thermal strain. Since the shell nosetip is generally designed for minimum wall thickness, burn-through of the forward shell or sidewall can result from excessive surface recession (ablation uncertainties, perturbed trajectory, and angle of attack). Local over-loading and/or lateral shifting of a shell nosetip can result from mismatches in radial growth between segmented wedge supports and the surrounding graphite shell. In addition, a thin shell can allow external boundary-layer gases to leak into and through the shell owing to the open porosity of crystalline graphite. Shape-change of a plug nosetip can adversely effect downstream heatshield ablation. Also, a plug nosetip can lose lateral support and shape stability near the plug-heatshield interface due to indepth and backface thermal decomposition of the surrounding heatshield which is used to hold and support the high-temperature graphite plug.

Generally the most critical mode of failure for graphite nosetips is fracture caused by excessive thermal strains that develop during re-entry (the majority of predicted peak flight strains lie between 0.3 and 0.4%—near the maximum strain allowables for average graphite billet material). Fracture can initiate along the inner surface of a shell nosetip or along the axis in the thicker portion of a plug configuration. The pattern of these tensile cracks may be longitudinal or circumferential depending on direction of maximum strain and on material capability.

Thermal Structural Response Model

First-iteration re-entry trajectories are based on initial nosetip shape, assuming the nosetip is completely shape stable at zero angle of attack. These trajectory data are input to a transient, axisymmetric (two-dimensional), finite-difference thermal code[6] which computes the shape-coupled thermal environment and resulting instantaneous nosetip shape and in-depth temperature field. If shape changes are sufficient to significantly alter drag, a second iteration on trajectory is performed. Final converged sets of instantaneous shapes, pressures, loads, and temperature fields at discrete altitudes are stored on tape and automatically input into a structures code that calculates stress, strain, and deformation data of interest.

The major uncertainties in thermal response concern input data on boundary-layer transition and graphite ablation. Figure 2 shows the general range of transition-onset data deduced from ground and flight tests.[1,10] Most flight transition data are derived from nosetip sidewall sensors (high M_e), and uncertainty exists in applying these data to the forward nosetip region (low M_e) where the major shape changes occur. Nosetip strain sensitivity studies have been made with various limiting transition criteria, ranging from constant $Re_{\theta,c}$ values to the Mach number dependent curves shown in Fig. 2. Once transition occurs, a variable transitional heating function is used to span the pure smooth-wall laminar and fully developed smooth-wall turbulent heating regimes.

Figure 3 gives a comparison of the mass-transfer parameter B_w' for carbon sublimation (ratio of carbon mass flux to blowing heat-transfer coefficient) and resulting surface temperature t_w and ablation rate $\dot{s}$ from a number of contemporary theories.[7,11-13] While each equilibrium model depends essentially on the same boundary-layer mass- and energy-transfer assumptions, differences exist in the reaction system adopted and in the thermodynamic properties assigned to the various ablation species. The kinetic rate-controlled model[11] assumes that reaction kinetics are not infinitely fast. This theory is therefore more appealing, except for its uncertainties in vaporization coefficients.[14] None of the models is conclusively substantiated by experimental data, one difficulty being that mechanical erosion cannot be separated from pure chemical ablation at the high pressures of interest.

At elevated pressures measured graphite recession rates begin to depart from pure chemical erosion due to mechanical loss effects. Figure 4 shows two mechanical erosion models used in the nosetip design sensitivity studies. According to I, chemical erosion alone controls surface recession at all locations along the nosetip where $p \leq 55$ atm, while at

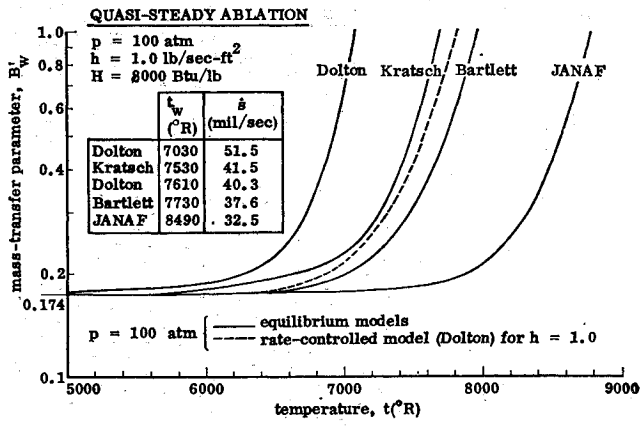

Fig. 3 Chemical ablation models for graphite.

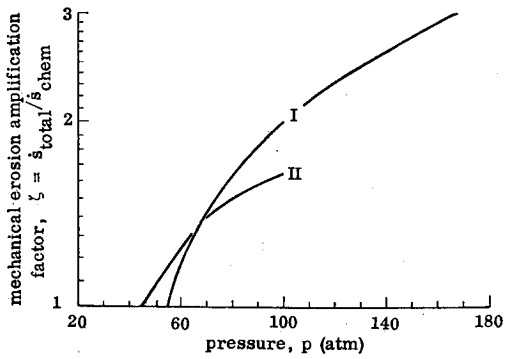

Fig. 4 Mechanical ablation models for graphite.

locations where $p > 55$ atm mechanical erosion combines with chemical ablation to amplify total surface recession. At $\zeta = 3$, e.g., the mechanical erosion rate is twice the chemical rate. The thermal response model for graphite (using I) has been exercised over a broad range of ballistic re-entry conditions V_E and γ_E and vehicle characteristics R_N and $\bar{\beta}$. Calculated data and flight-test measurements on total stagnation-point recession at impact are reasonably well correlated by an equation of the general dimensionless form

$$s/R_N = a(\lambda - 1) + b; \qquad 1 \leq \lambda \leq 1000$$

where a and b are constants.

Figure 5 gives representative thermal and mechanical properties of graphite used in design calculations of thermal and structural response. Except for specific heat c, the properties of thermal conductivity k, thermal expansion β, elastic modulus E, and Poisson ratio ν are directionally dependent owing to the oriented grain structure of graphite. The bounding curves give uniaxial properties that have been measured along the orthogonal directions across and with grain.

Thermal strains in a graphite nosetip at zero angle of attack are calculated by an elastic/plastic, axisymmetric, finite-element scheme[15] which automatically generates a new grid for the ablated shape at successive altitudes. The code includes three different quadrilateral linear strain elements, an eight degree-of-freedom isoparametric element and two modified isoparametric elements for improved bending response. Inputs to the code include orthotropic material properties (Fig. 5). Solutions of the linear simultaneous network equations are obtained by gaussian elimination techniques for determination of stresses, strains, and displacements throughout the finite-element model. An iterative scheme is

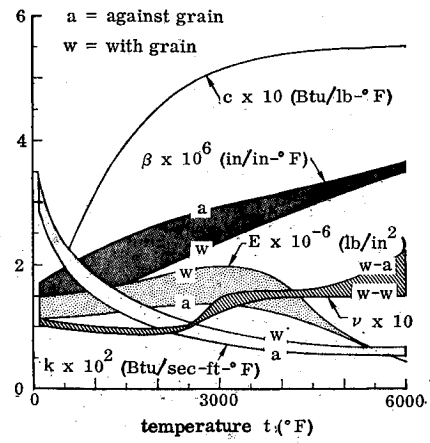

Fig. 5 Thermal and mechanical properties of graphite.

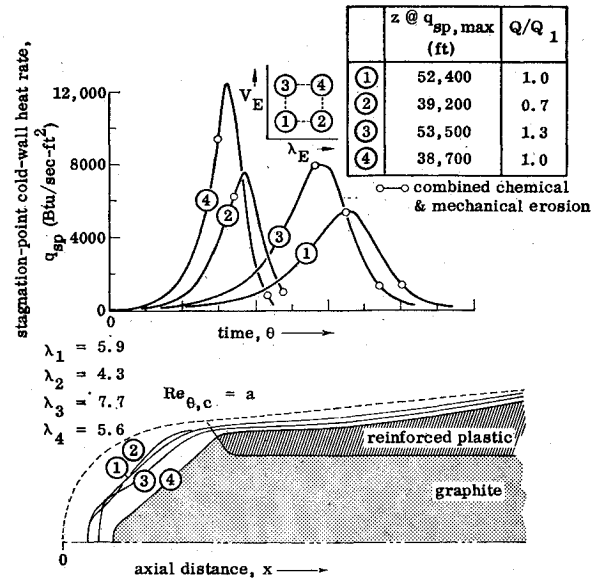

	z @ $q_{sp,max}$ (ft)	Q/Q_1
①	52,400	1.0
②	39,200	0.7
③	53,500	1.3
④	38,700	1.0

Fig. 6 Effect of trajectory on impact of plug/heatshield combination.

used to account for differences between tensile and compressive properties. Owing to inadequate material characterization, only the linear elastic portion of the structures code has been used here.

Thermal Structural Performance Predictions

Plug Design

Figure 6 gives stagnation-point heating history and combined nosetip/heatshield ablation contours at impact for a blunt graphite plug nosetip exposed to initial re-entry conditions represented by the four corners of a rectangular V-γ map. The ablation contours were obtained by a coupled calculation using a quasi-steady shape-change code[16] modified for two ablative materials. At high velocity V_E both plug and heatshield recessions are sensitive to γ_E.

Figure 7 shows instantaneous shape and indepth isotherms

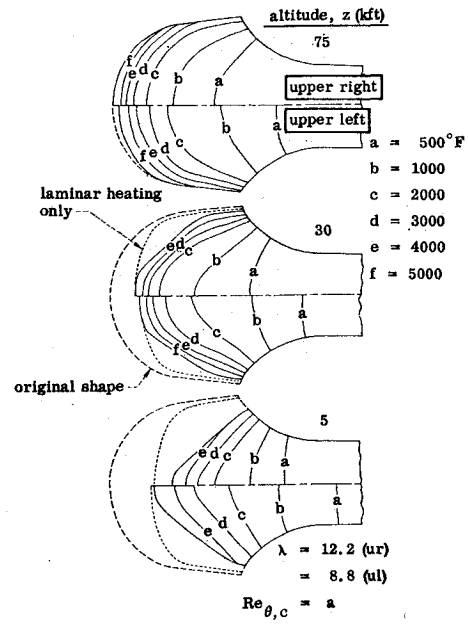

Fig. 7 Effect of trajectory on shape and temperature response of a graphite plug nosetip.

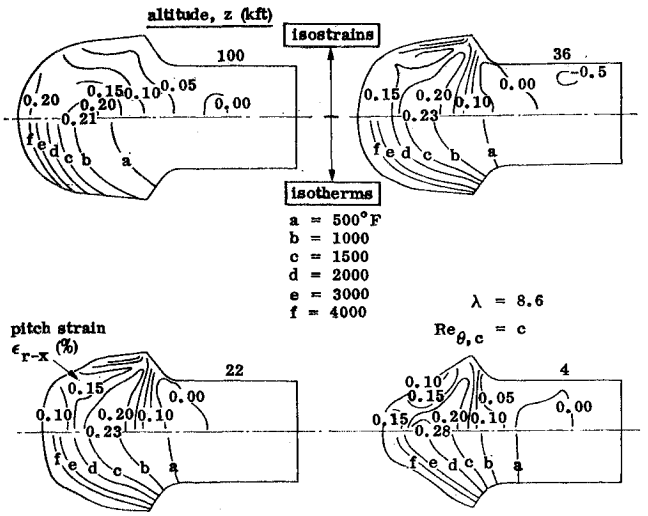

Fig. 8 Isotherms and isostrains in a graphite plug nosetip.

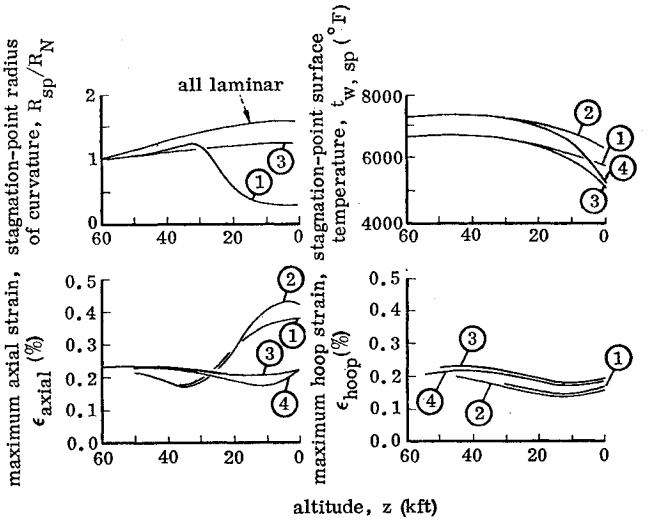

Fig. 9b Concluded: surface characteristics and thermal strains.

in a blunt graphite plug nosetip for upper-right (steep re-entry) and upper-left (shallow re-entry) trajectories and early boundary-layer transition (BLT). Although stagnation-point recession in the steep case lags that for shallow re-entry at medium altitudes, it catches up near 25 *k*ft and exceeds shallow re-entry at impact. Plug shank temperatures are higher (5000°F forward lip) for upper left due to prolonged conduction time.

Figure 8 gives isotherms and corresponding isostrains in the r-x (pitch) plane of a graphite plug nosetip for variable (delayed) BLT. Maximum tensile strains develop along the plug centerline, their peaks occurring near impact.

Figure 9a shows instantaneous surface contours and location of BLT on a graphite plug nosetip as effected by transition criteria (Fig. 2) and by combinations of chemical erosion model (Dolton or Bartlett, Fig. 3) and mechanical erosion model (I or II, Fig. 4). Figure 9b gives additional comparisons for these modeling assumptions. Effective nosetip radius of curvature effects aerodynamics through nosetip pressure drag. Progressive stagnation-point blunting develops if no transition occurs. Blunting in the stagnation region also develops for variable transition while early transition causes abrupt sharpening at low altitudes. Surface temperatures depend on ablation model at high altitudes and on transition model at low altitudes. The maximum axial and hoop strains in the plug are relatively insensitive to ablation model and depend mostly on transition criterion. Delayed BLT markedly reduces maximum axial strain and causes a slight increase in maximum hoop strain; this changes the potential failure mode from radial to axial cracks.

Figure 10 gives the history of maximum axial and hoop strains in a graphite plug nosetip for re-entry at the four corners of a V-γ map. Trajectory effects on thermal strain are delayed to low altitudes in the plug configuration. The peaks in axial strain are higher when re-entry velocity and/or angle is increased. Both the maximum axial and maximum hoop strains fall off at low altitudes for shallow re-entry, owing to the plug becoming more isothermal during the longer heating periods of low γ_E.

Rocket-exhaust exposure tests of full-scale plug graphite nosetips have produced thermal strain failures when the test environment (oxygen-to-fuel ratio) was adjusted to generate theoretical strains at or above $\epsilon = 0.5\%$. Large plug overhang δ (Fig. 18) favors forward heatshield performance but produces high axial strain and radial cracking. This fracture mode has also been confirmed by the rocket-exhaust tests.

Shell Design

Figure 11 shows isotherms and corresponding isostrains in a blunt graphite shell nosetip having an elliptical inner surface contour. Maximum strains develop in the vicinity of the ellipse/cone tangency point; peak values occur near 54 *k*ft and decrease at lower altitudes where temperature gradients diminish and the shell becomes more nearly isothermal.

Figure 12 gives the results of a linear elastic solution for biaxial strains along the inner surface of a graphite shell nosetip (arrows on each curve indicate direction from stagnation point proceeding aft). Maximum strains occur in the across-grain direction at 49 *k*ft. A nearly one-to-one ratio of biaxial strains develop along the inner surface. These data are to be

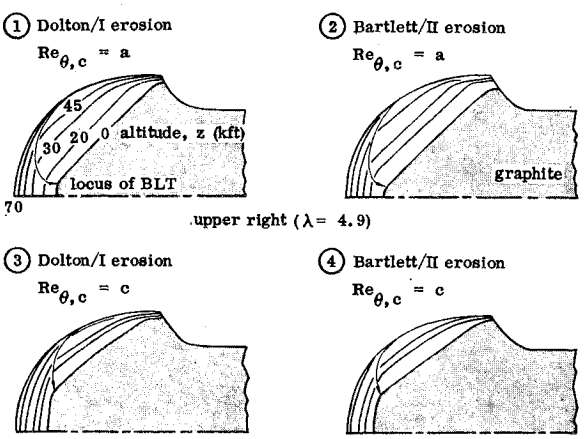

Fig. 9a Effect of chemical/mechanical ablation model and transition on graphite plug nosetip: shape history.

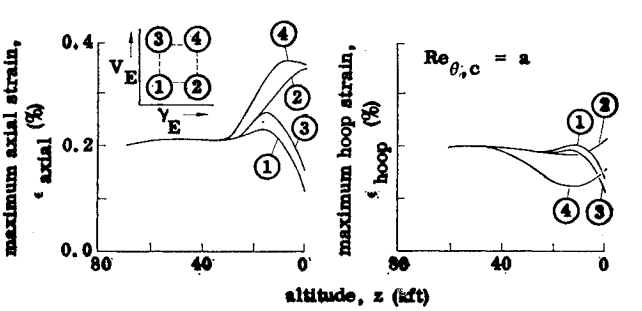

Fig. 10 Effect of trajectory on history of maximum strains in a graphite plug nosetip.

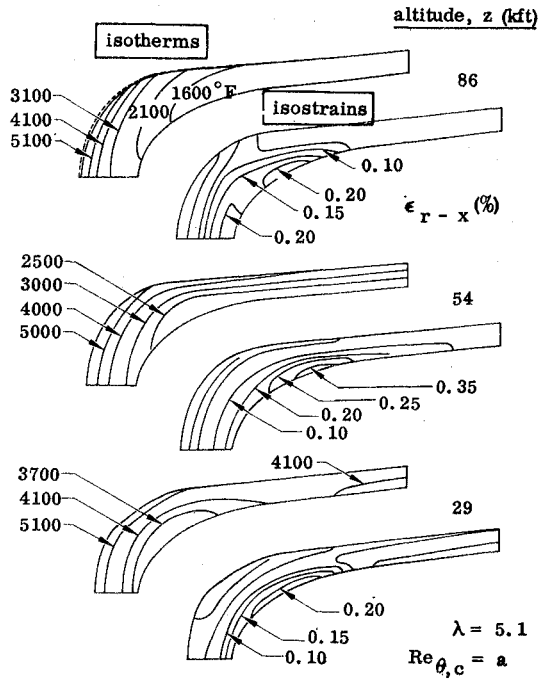

Fig. 11 Isotherms and isostrains in a graphite shell nosetip.

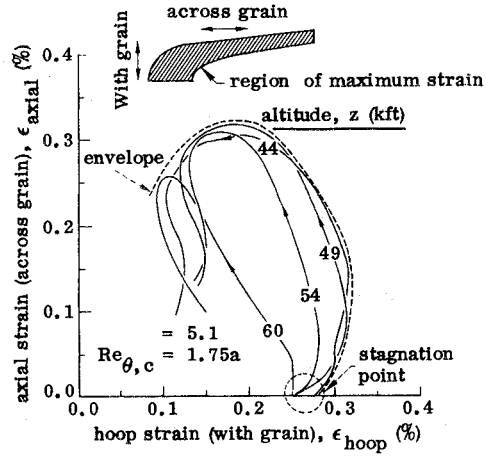

Fig. 12 Biaxial strains in a graphite shell nosetip.

compared with a maximum strain failure criterion to establish nosetip survival. Figure 13 gives an example criterion based on measured biaxial strain failure on a limited number of graphite billets.[17]

The effect of BLT on maximum thermal strains in a sharp graphite shell nosetip is illustrated in Fig. 14. As transition

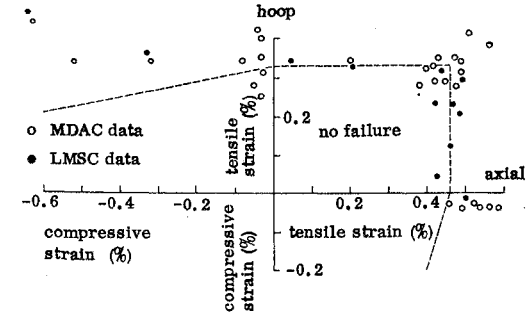

Fig. 13 Example biaxial strain allowables for graphite.

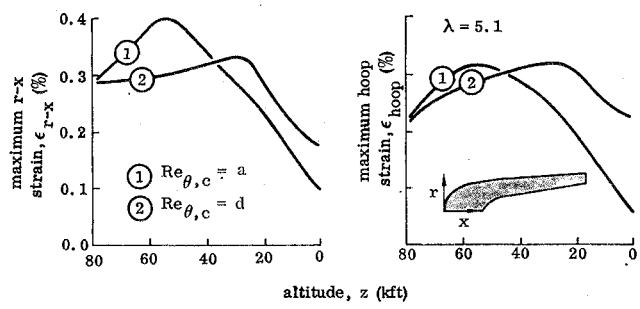

Fig. 14 Effect of transition on history of maximum strains in a graphite shell nosetip.

criterion is changed from a constant (early) $Re_{\theta,c}$ to a variable (delayed) $Re_{\theta,c}$, peak strains move from tangency region toward the stagnation point. The peak in r-x strain history is delayed and decreased, while in the hoop direction this peak is delayed and increased. Thus, transition can effect both failure mode and fracture direction.

Figure 15 shows history of maximum tensile strain (r-x or hoop near inner stagnation point) in a blunt graphite shell nosetip as a function of initial re-entry conditions. Increasing either or both V_E and γ_E generally increases the peak in maximum strain. The variation in these peak tensile strains across the V-γ map is shown in Fig. 16 for two

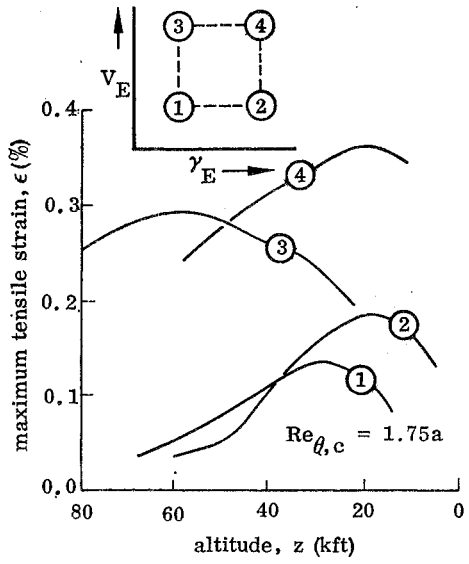

Fig. 15 Effect of trajectory on history of maximum strains in a graphite shell nosetip.

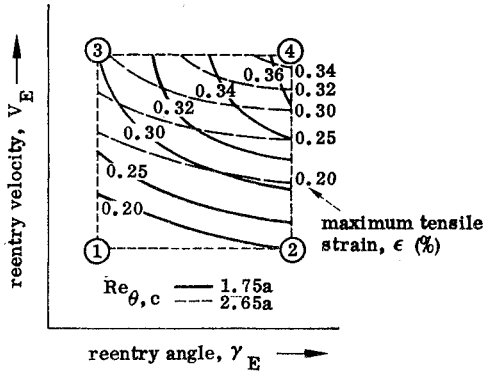

Fig. 16 Effect of transition on V-γ isostrain map for a graphite shell nosetip.

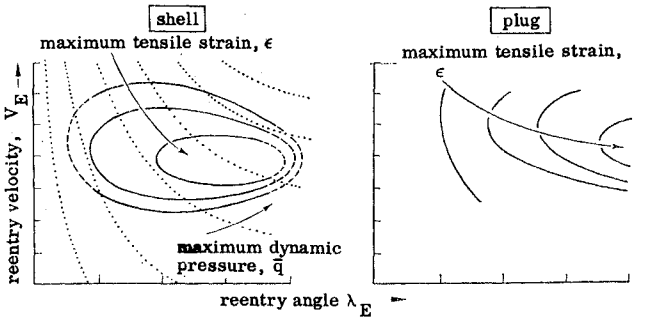

Fig. 17 V-γ **isostrain maps for graphite shell and plug nosetips.**

constant transition criteria. Later transition (larger $Re_{\theta,c}$) reduces the peak strain, the relief being larger in the middle of the V-γ map than at either the upper-left or upper-right corners.

A summary of more extensive calculations for shell and plug nosetips is given in the isostrain V-γ plots of Fig. 17. Although an increase in either V_E or γ_E generally increases maximum tensile thermal strains, there are conditions where the relieving effects of erosion and external air pressure (dotted curves) overtake the increasing thermal strain. The net result is that strains begin to diminish rather than increase indefinitely. This causes the peak thermal strain to occur at some point in the central region of the V-γ map, and so isostrain lines become elliptical in shape. Thus, at more severe re-entry conditions, thermal strain can become less critical and other nosetip failure modes can dominate.

Special Design Problems

Heatshield Response with Plug Nosetip

The choice of plug overhang entails a design compromise. While thermal strains are minimized by small plug overhang, increasing δ eliminates a forward-facing plug/heatshield interface, minimizes plug/heatshield ablation mismatch, and minimizes downstream heatshield ablation (Fig. 18). For larger overhangs δ/R_N, the graphite plug shields the afterbody and maximum heatshield ablation occurs downstream of the material discontinuity ("coke bottle" shape change).

Figure 19 shows progressive ablation and indepth decomposition of a plastic heatshield used with a blunt graphite plug nosetip. Also shown are instantaneous temperature profiles through the surviving heatshield. High interface temperatures can cause local heatshield decomposition and aggravated ablation effects near the material discontinuity. In addition, backface heatshield charring occurs due to contact with the hot plug shank. Decomposition gases must be vented through this developing char layer. At low altitudes the outer heatshield begins to cool while the temperature of its inner

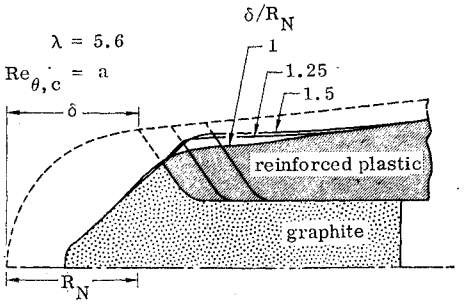

Fig. 18 Effect of plug overhang δ **on heatshield ablation.**

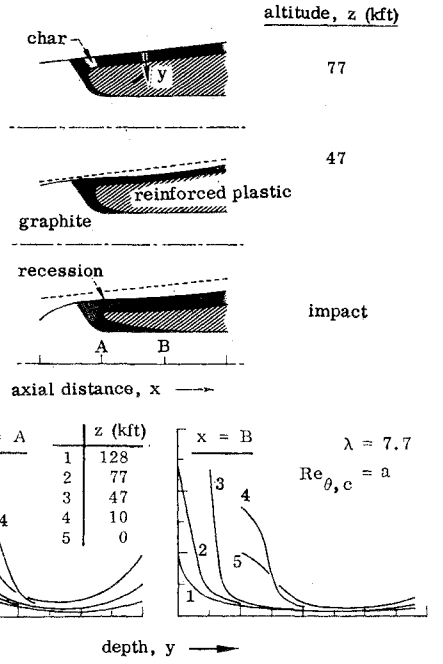

Fig. 19 Heatshield decomposition with a graphite plug nosetip.

surface continues to rise. This can cause aggravated thermal stresses and local failures in the degraded and pressurized forward heatshield region.

Thermal Growth of Shell Nosetip

The need to maintain lateral support while the nosetip is continuously expanding represents a critical requirement to satisfy in shell nosetip designs. Relative axial growth at the inner stagnation point and radial growth at the sidewall attachment region are shown in Fig. 20, along with required axial movement of the supporting wedge. This segmented wedge is spring loaded in the axial direction to insure that it slides forward during nosetip assembly and during heatup, thereby providing continuous lateral support throughout re-entry.

Flow through Shell Nosetip

As a result of the finite open porosity of graphite, a small fraction of high-pressure external flow can leak into the graphite shell and penetrate the shell cavity. This can cause internal oxidation of the porous shell (degrading mechanical properties), superimpose pressure strains on existing thermal strains in the shell, and pressurize the cavity (aggravating

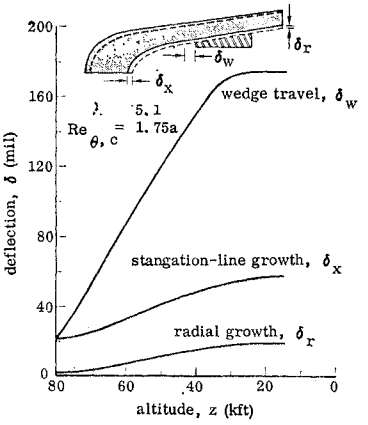

Fig. 20 Thermal growth of a graphite shell nosetip.

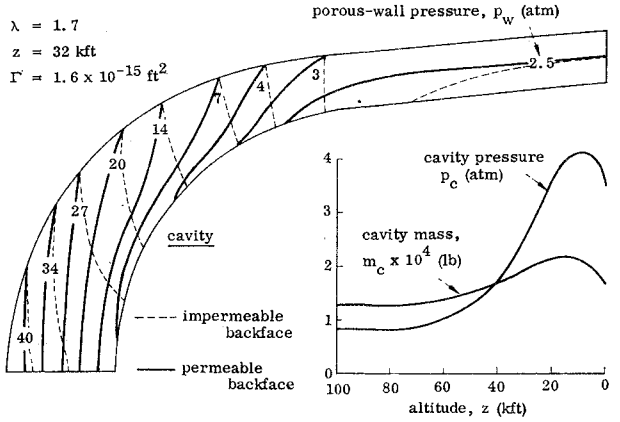

Fig. 21 Flow in a graphite shell nosetip.

attachment loads). Figure 21 shows example results from a transient compressible solution[18] for air ingestion during re-entry. The pressure field at 32 *k*ft is shown for a shell of uniform permeability whose backface is either permeable or impermeable. Also shown for the permeable case is cavity pressure and accumulated air mass in the cavity (accounting for leakage back out through the low-pressure sidewall) down to impact. The mass flow rates in the shell itself are too small to affect the matrix temperature distribution, and as such shell thermal strains are perturbed only by pore pressure.

References

[1] Thyson, N. et al., "Nose Tip Shape Change Predictions during Atmospheric Re-Entry," AIAA Paper 70-827, Los Angeles, Calif., 1970.

[2] D. Cristina, V., "Hyperthermal Ablation Performance of Carbon-Carbon Composites," AIAA Paper 71-416, Tullahoma, Tenn., 1971.

[3] Kratsch, K. M. et al., "Carbon-Carbon 3-D Orthogonal Material Behavior," AIAA Paper 72-365, San Antonio, Texas, 1972.

[4] Welsh, W. E., Jr., "Shape and Surface Roughness Effects on Nosetip Ablation," *AIAA Journal*, Vol. 8, No. 11, Nov. 1970, pp. 1983–1989.

[5] Popper, L. A. et al., "Three-Dimensional Ablation Considering Shape Change and Internal Conduction," *AIAA Journal*, Vol. 8, No. 11, Nov. 1970, pp. 2071–2074.

[6] Chin, J. H., "Coupling of Shape Change, Heating Distribution, and Internal Conduction for Ablating Bodies," *AIAA Progress in Astronautics and Aeronautics: Fundamentals of Spacecraft Thermal Design*, Vol. 29, edited by J. Lucas, MIT Press, Cambridge, Mass., 1972, pp. 333–347.

[7] Kratsch, K. M. et al., "Graphite Ablation in High-Pressure Environments," AIAA Paper 68–1153, Williamsburg, Va., 1968.

[8] Auerbach, I. et al., "Recent Graphite Nosetip Developments," AIAA Paper 71-417, Tullahoma, Tenn., 1971.

[9] Lundell, J. H. and Dickey, R. R., "The Ablation of Graphite Materials in the Sublimation Regime," AIAA Paper 72-298, San Antonio, Texas, 1972.

[10] "Final Report, NDAT: Vol. I—Part I, Improvements in Environment and Materials Response Prediction Capabilities," B133378, Oct. 30, 1970, Lockheed Missiles & Space Co., Sunnyvale, Calif.

[11] Dolton, T. A., Goldstein, H. E., and Maurer, R. E., "Thermodynamic Performance of Carbon in Hyperthermal Environments," *AIAA Progress in Astronautics and Aeronautics: Thermal Design Principles of Spacecraft and Entry Bodies*, Vol. 21, edited by J. Bevans, Academic Press, New York, 1969, pp. 169–201.

[12] Bartlett, E. P., "Analytical and Graphical Prediction of Graphite Ablation Rates and Surface Temperatures During Reentry at 25,000 to 45,000 ft/sec," FTC-TDR-63-40, March 1964, Air Force Flight Test Center, Edwards Air Force Base, Calif.

[13] "JANAF Thermochemical Data," 1963, Dow Chemical Co., Midland, Mich.

[14] Welsh, W. E., Jr., "Proceedings of the Workshop on Graphite Ablation," Rept. TOR-0172(S2816-76)-11, Jan. 30, 1972, The Aerospace Corp., El Segundo, Calif.

[15] Stocks, B. B. and Cyr, N. A., "Finite Element Analysis of Re-Entry Vehicle Nosetips," D054092, Jan. 1972, Lockheed Missiles & Space Co., Sunnyvale, Calif.

[16] Gallagher, L. W., Coleman, W. D., and Hearne, L. F., "Final Report, NDAT: Vol. III, Computer User's Manual for the Contour Change of Ablating Nosetips (COCAN)," D030054, Dec. 15, 1970, Lockheed Missiles & Space Co., Sunnyvale, Calif.

[17] Jorner, J., "Multiaxial Behavior of Graphite," AFML-TR-71-253, Dec. 1971, McDonnell-Douglas Astronautics Co., Huntington Beach, Calif.

[18] Levy, C. N. and Reneau, L. R., "Pressure and Temperature Distributions Associated with Flow through a Porous Nosetip," IDC 81-11/1053, Feb. 29, 1972, Lockheed Missiles & Space Co., Sunnyvale, Calif.